








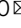


Photoinduced metastable *dd*-exciton-driven metal-insulator transitions in quasi-one-dimensional transition metal oxides

Teguh Citra Asmara^{1,2,3,12}[✉], Frank Lichtenberg^{4,12}, Florian Biebl^{5,6,12}, Tao Zhu⁷, Pranab Kumar Das¹, Muhammad Avicenna Naradipa^{1,7}, Angga Dito Fauzi^{1,7}, Caozheng Diao¹, Ping Yang^{1,8}, Philipp Lenzen^{5,6}, Sören Buchenau^{5,6}, Benjamin Grimm-Lebsanft^{5,6}, Dongyang Wan², Paolo E. Trevisanutto^{7,9}, Mark B. H. Breese^{1,7}, T. Venkatesan^{2,7,8,10,11}, Michael Rübhausen^{5,6}[✉] & Andrivo Rusydi^{1,2,7,9,10}[✉]

Photoinduced phase transitions in matters have gained tremendous attention over the past few years. However, their ultrashort lifetime makes their study and possible control very challenging. Here, we report on highly anisotropic *d-d* excitonic excitations yielding photoinduced metal-insulator transitions (MITs) in quasi-one-dimensional metals $\text{Sr}_{1-y}\text{NbO}_x$ using Mueller-Matrix spectroscopic ellipsometry, transient ultraviolet Raman spectroscopy, transient mid-infrared reflectivity and angular-resolved photoemission spectroscopy supported with density functional theory. Interestingly, the MITs are driven by photo-pumping of *d-d* excitons, causing the metallic *a*-axis to become insulating while the insulating *b*- and *c*-axis concomitantly become a correlated metal. We assign these effects to an interplay between the melting of charge and lattice orderings along the different anisotropic optical axes and Bose-Einstein-like condensation of the photoinduced excitons. The long lifetime in the order of several seconds of the metastable MITs gives greater flexibility to study and manipulate the transient excitonic state for potential applications in exciton-based optoelectronic devices.

¹ Singapore Synchrotron Light Source, National University of Singapore, Singapore 117603, Singapore. ² NUS Nanoscience and Nanotechnology Initiative, National University of Singapore, Singapore 117411, Singapore. ³ Photon Science Division, Paul Scherrer Institute, CH-5232 Villigen PSI, Switzerland. ⁴ Department of Materials, ETH Zurich, CH-8093 Zurich, Switzerland. ⁵ Institute of Nanostructure and Solid State Physics, University of Hamburg, 22761 Hamburg, Germany. ⁶ Center for Free-Electron Laser Science (CFEL), Luruper Chaussee 149, 22761 Hamburg, Germany. ⁷ Department of Physics, National University of Singapore, Singapore 117551, Singapore. ⁸ Department of Materials Science and Engineering, National University of Singapore, Singapore 117575, Singapore. ⁹ Centre for Advanced 2D Materials, National University of Singapore, Singapore 117546, Singapore. ¹⁰ National University of Singapore Graduate School for Integrative Sciences and Engineering, Singapore 117456, Singapore. ¹¹ Department of Electrical and Computer Engineering, National University of Singapore, Singapore 117583, Singapore. ¹² These authors contributed equally: Teguh Citra Asmara, Frank Lichtenberg, Florian Biebl. ✉email: teguh.asmara@psi.ch; mrbuehau@physnet.uni-hamburg.de; andrivo.rusydi@nus.edu.sg

Using light to manipulate fundamental physical properties of matter has gained tremendous attention in optical and condensed matter physics research. It has been shown that photoexcitation can induce transient exotic phases of matter that are not found in their equilibrium ground states. Examples, among others, include transient changes in crystal structures^{1,2}, ferroelectricity¹, metal-insulator transitions^{2–4} (MITs), melting of spin and charge orders^{5–7}, and even superconductivity^{8,9}. The most fundamental way in which light can interact with matter is by exciting electrons from occupied to unoccupied states, creating electron-hole pairs that can bind to form excitons. Thus, excitons are expected to play important roles in the dynamics of these transient phases of matter. Since excitons are bosons, high-density excitons created by high-intensity photoexcitation can potentially condense into transient Bose-Einstein condensates^{10–12} (BECs), similar to what has been demonstrated by photoinduced magnon BEC transition driven by high-intensity microwave pumping¹³. However, the main difficulty with excitons (and other transient states of matter in general) is their ultrashort lifetime, which is often in the pico- to femtosecond range. This short timescale renders it challenging to probe and control these transient states.

Here, using a combination of Mueller-matrix spectroscopic ellipsometry, steady-state and transient ultraviolet Raman spectroscopies, transient mid-infrared reflectance, and angular-resolved photoemission spectroscopy (ARPES) supported by theoretical calculations, we probe both the steady-state and dynamic dielectric responses of strongly anisotropic quasi-one-dimensional (quasi-1D) correlated metals $\text{Sr}_{1-y}\text{NbO}_x$ of the type $\text{A}_n\text{B}_n\text{O}_{3n+2}$ as a model system. We reveal that the photoinduced pumping of low-energy $d-d$ excitons in $\text{Sr}_{1-y}\text{NbO}_x$ dramatically changes their electronic, lattice, and optical properties. The $d-d$ exciton pumping is found to drive complementary MITs along different optical axes, where the metallic axis switches to become insulating while the insulating axis concomitantly becomes more metallic by rearranging their charge and lattice orderings. The excited state is metastable with an extremely long lifetime of several seconds, caused by the slow recovery of the changes in lattice orderings and possible emergence of BEC-like excitonic phase. This long lifetime gives greater flexibility in manipulating the pumped state for both fundamental research and practical applications.

Results

Anisotropic properties of $\text{Sr}_{1-y}\text{NbO}_x$. $\text{Sr}_{1-y}\text{NbO}_x$ is known to exhibit a rich phase diagram that strongly depends on the oxygen content¹⁴, ranging from isotropic metal SrNbO_3 (ref. 15), to a quasi-1D metal $\text{SrNbO}_{3.4}$ (refs. 16–20), and to ferroelectric insulator $\text{SrNbO}_{3.5}$ (ref. 21). Especially, the quasi-1D metal-like phases of $\text{Sr}_{1-y}\text{NbO}_x$ are ideal to study low-dimensional and MIT physics, as shown by their transition into an insulating charge density wave state at low temperatures^{17–19}. The crystal structures of $\text{Sr}_{1-y}\text{NbO}_x$ are of the type $\text{Sr}_n\text{Nb}_n\text{O}_{3n+2} = \text{SrNbO}_x$, which represents a homologous layered perovskite-related series where the structure type, n , depends on the oxygen content, x . Along the c -axis, networks of NbO_6 octahedra are periodically grouped into n -octahedra thick slabs, while along the a - and b -axis the Nb–O–Nb bonds are chain-like and zig-zag-like, respectively¹⁴. For example, along the c -axis the slabs are 5-octahedra thick in $n = 5$ type $\text{SrNbO}_{3.4}$ (Fig. 1a, b), alternately 4- and 5-octahedra thick in $n = 4.5$ type $\text{SrNbO}_{3.45}$, and unlimited in isotropic perovskite $n = \infty$ type SrNbO_3 . The chain-like bonds facilitate the metallicity along the a -axis, while the zig-zag-like bonds and slab structures hinder the charge hoppings between Nb ions along the b - and c -axis, respectively, making them more insulating. This

arrangement makes $\text{Sr}_{1-y}\text{NbO}_x$ highly biaxially anisotropic, yielding an anisotropic dielectric tensor with different components of the complex dielectric function ϵ along different orthogonal optical axes. Thus, before probing their transient dynamical response, their steady-state diagonalized anisotropic dielectric tensors need to be determined using Mueller-matrix spectroscopic ellipsometry^{22–24}.

Mueller-matrix spectroscopic ellipsometry. Representative samples of $\text{Sr}_{0.95}\text{NbO}_{3.37}$ (an under-stoichiometric Sr- and O-deficient variant of $n = 5$ type $\text{SrNbO}_{3.4}$) and $n = 4.5$ type $\text{SrNbO}_{3.45}$ single crystals¹⁴ are measured using Mueller-matrix spectroscopic ellipsometry within the photon energy range of 0.38–6.10 eV at room temperature. The resulting real parts of principal ϵ of the samples, $\text{Re}[\epsilon]$, are shown in Fig. 1c–e. Along the a -axis, the $\text{Re}[\epsilon_a]$ spectra of both $\text{Sr}_{0.95}\text{NbO}_{3.37}$ and $\text{SrNbO}_{3.45}$ cross zero and become negative below 1.06 and 0.76 eV, respectively. In contrast, the $\text{Re}[\epsilon]$ of both samples along the b - and c -axes remain positive at all measured photon energies. This means both samples are metallic along the a -axis, but non-metallic along the b - and c -axes, indicating an intrinsic room-temperature quasi-1D metallic behavior consistent with previous electrical transport, ARPES, and infrared reflectivity results^{17–19}.

Figure 2a–c shows the imaginary parts of principal ϵ , $\text{Im}[\epsilon]$, of the samples, which are proportional to absorption spectra. These spectra also denote the quasi-1D metallicity of the samples, as shown by the presence of metallic Drude tail along the a -axis but not along the b - and c -axes. The Drude response contribution and the $\text{Re}[\epsilon_a]$ zero-crossing energy of $\text{Sr}_{0.95}\text{NbO}_{3.37}$ are higher than those of $\text{SrNbO}_{3.45}$, indicating a larger carrier density in $\text{Sr}_{0.95}\text{NbO}_{3.37}$ than in $\text{SrNbO}_{3.45}$ consistent with their nominal electronic structures¹⁴ ($\text{Nb-}4d^{0.16}$ for $\text{Sr}_{0.95}\text{NbO}_{3.37}$ and $\text{Nb-}4d^{0.10}$ for $\text{SrNbO}_{3.45}$).

In the $\text{Im}[\epsilon_b]$ and $\text{Im}[\epsilon_c]$ spectra (Fig. 2b, c) at low energies, three strong peaks are observed at ~ 0.7 and ~ 1.2 eV along the b -axis as well as at ~ 1.1 eV along the c -axis (Table 1). Interestingly, the intensities of these peaks are higher in $\text{Sr}_{0.95}\text{NbO}_{3.37}$ than in $\text{SrNbO}_{3.45}$, similar to the trends of the a -axis Drude response caused by the difference in the carrier density between the two samples. This reveals that the three peaks originate from the excitations of electrons, which are anisotropically-localized along the b - and c -axes but mobile along the a -axis. As discussed below (Fig. 3a), this is indeed the case; more precisely, the three peaks originate from $d-d$ transitions between split Nb- $4d$ bands across the Fermi level along the b - and c -axes. Thus, we name these three peaks as the $d-d$ excitations.

At higher energies, a distinct absorption edge is seen in the $\text{Im}[\epsilon]$ spectra along the a - and b -axes at ~ 4.4 eV for $\text{Sr}_{0.95}\text{NbO}_{3.37}$ and ~ 4.2 eV for $\text{SrNbO}_{3.45}$ due to the $\text{O-}2p \rightarrow \text{Nb-}4d$ charge-transfer inter-band transitions (see “Discussion” below). Meanwhile, in the intervening energy range of 2–4 eV the $\text{Im}[\epsilon_a]$ and $\text{Im}[\epsilon_b]$ of both samples are very close to zero, signifying the visible-range transparency of both samples along the a - and b -axes. In contrast, the $\text{Im}[\epsilon_c]$ spectra of both samples are quite absorbing above the $d-d$ excitations, characterized by the presence of several wide “humps” at varying energy positions (Table 1). Between the two samples, the overall intensities of these humps remain relatively the same (unlike the $d-d$ excitations), indicating that these humps do not originate from carrier excitations. Instead, based on the crystal structure in Fig. 1a, b, these humps could be caused by the presence of extra O layers every few unit cells along the c -axis that create new occupied and unoccupied states that contribute to the optical absorption and modulate the shapes of ϵ_c .

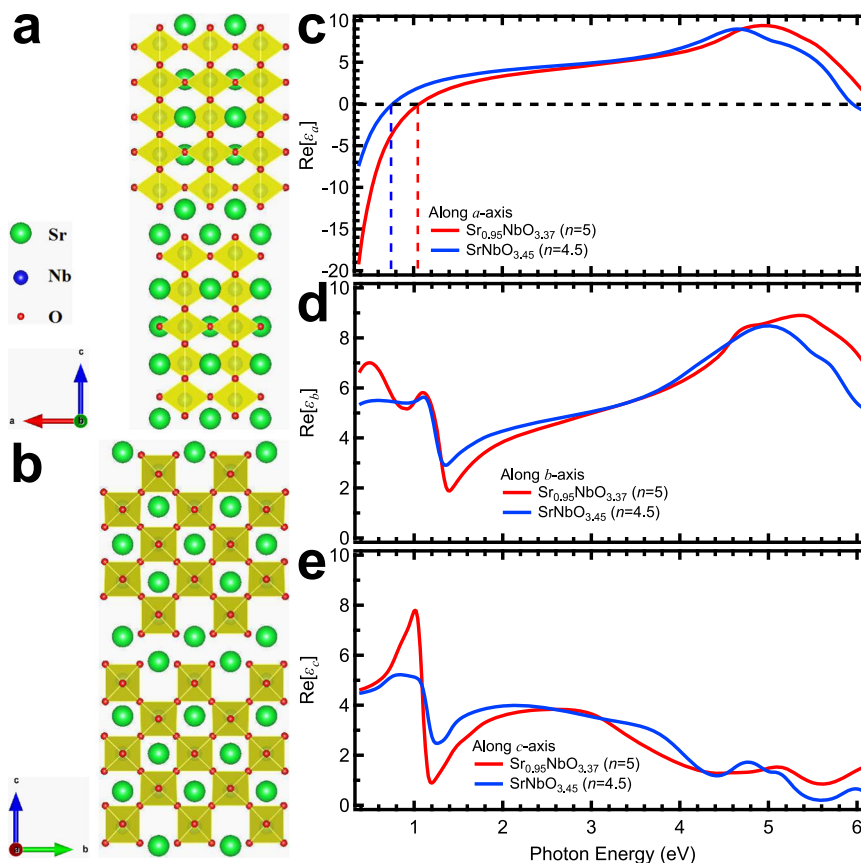


Fig. 1 Crystal structure and real part of complex dielectric functions of $\text{Sr}_{1-y}\text{NbO}_x$. **a** Crystal structure of $n=5$ type $\text{SrNbO}_{3.4}$ as a representative case projected on the orthorhombic ac plane (Sr = green, Nb = blue, O = red, NbO_6 octahedra = yellow). **b** Crystal structure of $\text{SrNbO}_{3.4}$ projected on the orthorhombic bc plane. **c** Real part of complex dielectric function, $\text{Re}[\epsilon]$, spectra of $n=5$ type $\text{Sr}_{0.95}\text{NbO}_{3.37}$ and $n=4.5$ type $\text{SrNbO}_{3.45}$ single crystal samples along the a -axis. Red and blue dashed lines denote the $\text{Re}[\epsilon]$ zero-crossing of $\text{Sr}_{0.95}\text{NbO}_{3.37}$ and $\text{Sr}_0\text{NbO}_{3.45}$, respectively. **d** The $\text{Re}[\epsilon]$ spectra of the samples along the b -axis. **e** The $\text{Re}[\epsilon]$ spectra of the samples along the c -axis.

Excitonic ultraviolet Raman spectroscopy. To further probe these $d-d$ excitations, we perform excitonic ultraviolet Raman spectroscopy (Fig. 2b inset) on the $n=5$ type $\text{Sr}_{0.95}\text{NbO}_{3.37}$ sample with an incoming beam of 240 nm (5.17 eV), i.e., on the onset of the $\text{O-}2p \rightarrow \text{Nb-}4d$ charge-transfer inter-band transitions. Along the b -axis, we find an excitonic peak centered at 0.89 eV Raman shift consistent with the lower $d-d$ excitation, indicating the excitonic nature of these $d-d$ excitations. Interestingly, a similar excitonic peak is also found at 0.86 eV along the a -axis, which means that the lower $d-d$ exciton also occurs along the metallic axis. In conventional metals, excitons are usually absent. Despite this, excitons are present in $\text{Sr}_{1-y}\text{NbO}_x$ because they are not conventional metals but rather correlated quasi-1D metals. In the $\text{Im}[\epsilon_a]$ obtained from Mueller-matrix ellipsometry, the a -axis $d-d$ exciton is overshadowed by the Drude response of the correlated electrons in the metallic direction (see Fig. 2a), and the use of Raman spectroscopy allows us to resolve the exciton since Drude excitations are usually invisible in optical Raman.

Electronic band structure. To determine the origins of the peaks in $\text{Im}[\epsilon]$ spectra, we calculate the electronic band structure of $n=5$ type $\text{SrNbO}_{3.4}$ (which is closely related to $n=5$ type $\text{Sr}_{0.95}\text{NbO}_{3.37}$ and $n=4.5$ type $\text{SrNbO}_{3.45}$) using density functional theory in Fig. 3a. The results are consistent with both experimental ARPES and ultraviolet photoemission (UPS) results and previous theoretical calculations^{17,19,20}. The band structure is plotted along the high symmetry lines of Γ - X (along the a -axis), Γ - Y (b -axis), and Γ - Z (c -axis) to determine the possible valence

and conduction band pairings that contribute to the $\text{Im}[\epsilon]$ spectra along each axis. The results show that the valence bands have mainly $\text{O-}2p$ character while the conduction bands have mainly $\text{Nb-}4d$ character, and together they contribute to the $\text{O-}2p \rightarrow \text{Nb-}4d$ charge-transfer inter-band transition edges.

Although the $\text{Nb-}4d$ bands are mostly unoccupied and lie above the Fermi level, a small group of $\text{Nb-}4d$ bands (red bands in Fig. 3a) cross the Fermi level, E_F , along Γ - X and lie occupied below it at Γ , along Γ - Y , and along Γ - Z . The strong dispersion and E_F crossing along Γ - X are consistent with the samples' metallic behavior along the a -axis and responsible for the Drude response excitation. Meanwhile, at Γ , along Γ - Y , and along Γ - Z , these bands lie below the E_F with no significant dispersion, consistent with the samples' non-metallic behavior along the b - and c -axes. The low-energy excitonic peaks in $\text{Im}[\epsilon]$ spectra can then be assigned to the transitions (green arrows in Fig. 3a) from these shallow occupied bands to the low-lying unoccupied bands at Γ , along Γ - Y , and along Γ - Z (blue bands in Fig. 3a). As both occupied and unoccupied bands have $\text{Nb-}4d$ character, these low-energy peaks are $d-d$ excitations. Although $d-d$ transitions are dipole forbidden in centrosymmetric compounds, they are distinctly observed here due to the symmetry breaking caused by the layered perovskite structure. Thus, the Drude response and the $d-d$ excitons originate from the same group of $\text{Nb-}4d$ bands, but along different directions in the reciprocal Brillouin zone and thus the real space.

Furthermore, we also perform room-temperature ARPES on the $\text{Sr}_{0.95}\text{NbO}_{3.37}$ sample to verify the band structure calculations.

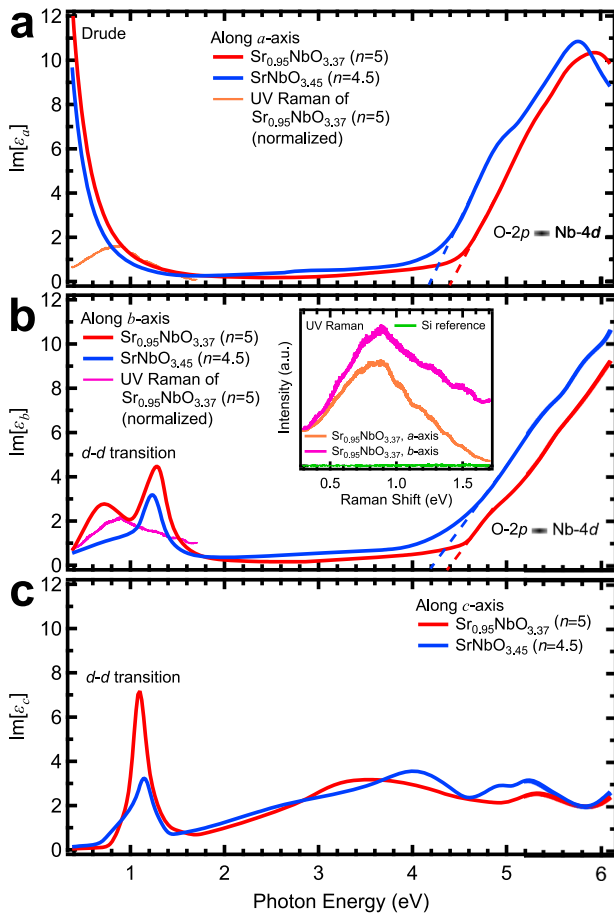


Fig. 2 Imaginary part of complex dielectric functions and ultraviolet Raman spectra of $\text{Sr}_{1-y}\text{NbO}_x$. **a** Imaginary part of complex dielectric function, $\text{Im}[\epsilon]$, spectra of $n = 5$ type $\text{Sr}_{0.95}\text{NbO}_{3.37}$ and $n = 4.5$ type $\text{SrNbO}_{3.45}$ single crystal samples along the a -axis. **b** The $\text{Im}[\epsilon]$ spectra of the samples along the b -axis. **c** The $\text{Im}[\epsilon]$ spectra of the samples along the c -axis. Red and blue dashed lines denote the linearly extrapolated O-2p \rightarrow Nb-4d charge-transfer inter-band transition edges of $\text{Sr}_{0.95}\text{NbO}_{3.37}$ and $\text{SrNbO}_{3.45}$, respectively. Inset is excitonic ultraviolet (UV) Raman spectra of the samples along the a - and b -axes. These spectra, normalized with respect to the d - d transition peaks along the b -axis, are also superimposed on the main panels to directly compare them with the $\text{Im}[\epsilon]$ spectra. For reference, the UV Raman spectrum of Si is also shown.

Figure 3b shows the band dispersion of the low-lying occupied Nb-4d bands along the X - Γ - X direction. We see two dispersing bands along Γ - X direction crossing the Fermi level indicative of its metallic behavior. We observe two arms of the parabolic band (as obtained from the first-principles calculations, see Fig. 3a), while the ARPES intensity at the Γ point is not visible. This discrepancy could be due to the photoelectric matrix element for the chosen photon energy; however, it does not affect our main discussion. The iso-energy Fermi surface is shown in Fig. 3c. The Fermi surface is highly anisotropic; it is elongated along the Y - Γ - Y direction while restricted along the X - Γ - X direction. We see two parallel linear features, which are characteristic for their unidirectional electronic structure.

Modulation of transient reflectance by d - d excitation. As the d - d excitons originate from the same bands of electrons (red bands in Fig. 3a) as the metallic Drude response, their excitations by polarized light can modulate the free electrons along the a -axis. To demonstrate this, we build a laser-based mid-infrared

Table 1 Optical excitation peaks along the three optical axes of $\text{Sr}_{1-y}\text{NbO}_x$.

Peak name	Energy (eV)	
	$\text{Sr}_{0.95}\text{NbO}_{3.37}$ ($n = 5$)	$\text{SrNbO}_{3.45}$ ($n = 4.5$)
Along a -axis		
Drude	0	0
O-2p \rightarrow Nb-4d	4.4	4.2
Along b -axis		
d - d transition	0.72	-
d - d transition	1.28	1.24
O-2p \rightarrow Nb-4d	4.4	4.2
Along c -axis		
d - d transition	1.10	1.14
Hump	3.5	4.0
Hump	5.3	4.96, 5.24

The energy position of each peak is determined from their respective apparent maxima, except for O-2p \rightarrow Nb-4d peaks where it is determined from their respective linearly extrapolated edge instead.

(MIR) pump-probe reflectance setup (Fig. 4a) and perform room-temperature transient pump-probe reflectivity experiments with fully controlled anisotropic polarizations on the $\text{Sr}_{0.95}\text{NbO}_{3.37}$ sample. The sample is pumped with polarization parallel to the b -axis ($\mathbf{E}_{\text{pump}} // b$ -axis) at 1030 nm wavelength (~ 1.20 eV) and 600 Wcm^{-2} power density to excite the d - d excitons along the b -axis, and then probed with polarization parallel to the a -axis ($\mathbf{E}_{\text{probe}} // a$ -axis) at 7 μm wavelength (~ 0.18 eV) to observe the effects of the d - d excitations on the transient reflectance along the metallic a -axis, $R_{\text{trans}}(a)$. The result in Fig. 4b shows that upon turning on the pump beam, $R_{\text{trans}}(a)$ drastically decreases all the way down to the steady-state reflectance of the non-metallic b -axis, R_b , indicating a near-100% switching from metal to insulator. When the pump beam is turned off, $R_{\text{trans}}(a)$ recovers back to the steady-state metallic level, R_a , indicating a relaxation toward the initial state. The relaxation times of the pump-on and pump-off conditions are found to be in the order of several seconds; in this particular orientation, they are fitted to be 5.8 ± 0.2 s and 4.6 ± 0.2 s, respectively.

As the optical response of the a -axis within the MIR range is dominated by the metallic Drude response^{18,19}, a decrease in its MIR transient reflectance indicates a decrease of the Drude peak, which directly translates to a decrease in the carrier density²³. Thus, the drastic, nearly 100% decrease of $R_{\text{trans}}(a)$ toward the steady-state insulating level in Fig. 4b is strongly suggesting an exciton-driven transient metal-insulator transition (MIT), indicating a photoinduced switching capability of $\text{Sr}_{1-y}\text{NbO}_x$.

To prevent excessive heat damage, in Fig. 4c $n = 5$ type $\text{Sr}_{0.95}\text{NbO}_{3.37}$ is pumped with a lower power density of 260 Wcm^{-2} , which results in lower decrease of $R_{\text{trans}}(a)$ but excellent repeatability of the switching. Intriguingly, when $\mathbf{E}_{\text{probe}}$ is parallel to the b -axis, the 1.2 eV d - d exciton pumping causes an increase of the transient reflectance (and thus the metallicity) along the b -axis, $R_{\text{trans}}(b)$. This means that while the exciton pumping is switching the metallic a -axis to be more insulating, it also concomitantly switches the insulating b -axis to be more metallic (i.e., insulator-metal transition or IMT), making the strongly anisotropic $\text{Sr}_{0.95}\text{NbO}_{3.37}$ effectively more isotropic. More evidence can be seen in the power density, P_{pump} , dependence of the switching in Fig. 4d, which shows that while $R_{\text{trans}}(a)$ decreases linearly with increasing P_{pump} , $R_{\text{trans}}(b)$ increases concomitantly instead, outlining charge conservation. The switching effect can also be observed when $\mathbf{E}_{\text{pump}} // a$ -axis due to the presence of the ~ 0.9 eV d - d exciton along the a -axis as

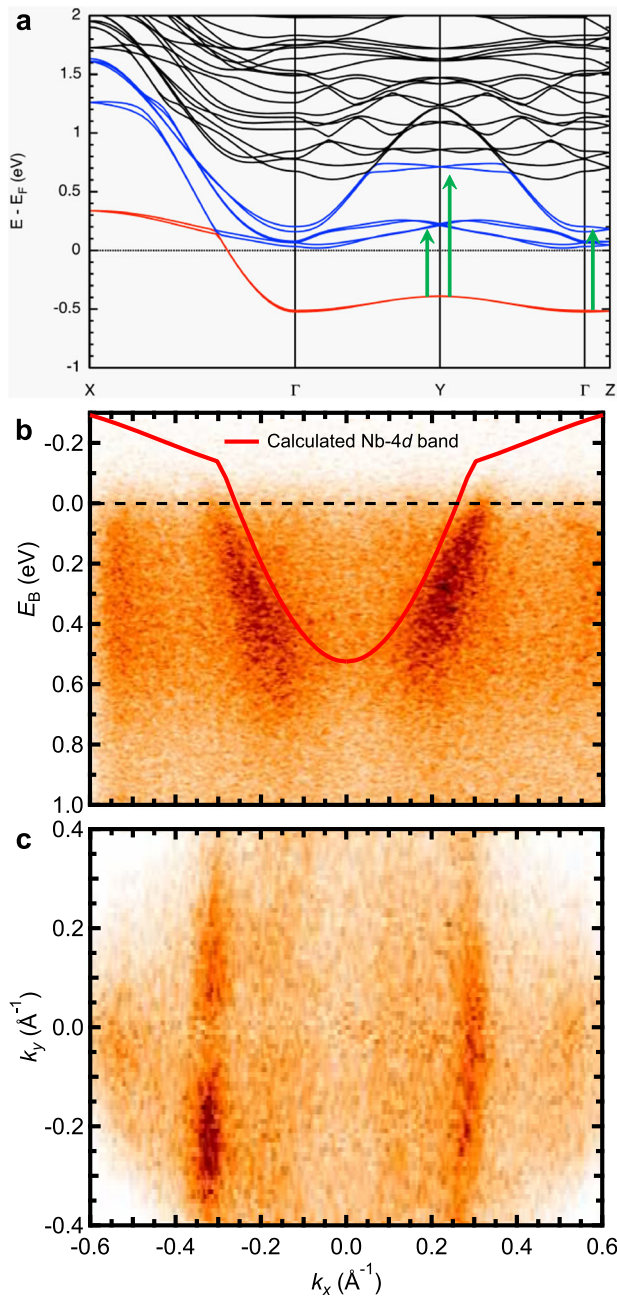


Fig. 3 Electronic band structure of $n = 5$ type $\text{Sr}_{1-y}\text{Nb}_y\text{O}_{3.4}$. **a** Theoretically calculated band structure of $n = 5$ type $\text{SrNbO}_{3.4}$. Red and blue bands denote the occupied and unoccupied Nb-4d bands responsible for the d - d transition peaks (green arrows), respectively. Black dotted line denotes the Fermi level energy, E_F . The red bands strongly disperse and cross E_F along the a -axis (Γ - X) but stay below it with little dispersion at Γ , along the b -axis (Γ - Y), and c -axis (Γ - Z). **b** Angular-resolved photoemission spectroscopy (ARPES) result of $n = 5$ type $\text{Sr}_{0.95}\text{NbO}_{3.37}$ sample along the a -axis (Γ - X). The theoretically calculated red Nb-4d band is superimposed for comparison. **c** Iso-energy Fermi surface map of $n = 5$ type $\text{Sr}_{0.95}\text{NbO}_{3.37}$ sample.

revealed by ultraviolet Raman spectroscopy (Fig. 2d), showing further evidence of the exciton-driven nature of the switching.

Transient pump-probe phononic ultraviolet Raman spectroscopy. Furthermore, to study the effect of the exciton pumping on the transient lattice and charge orderings, we perform transient

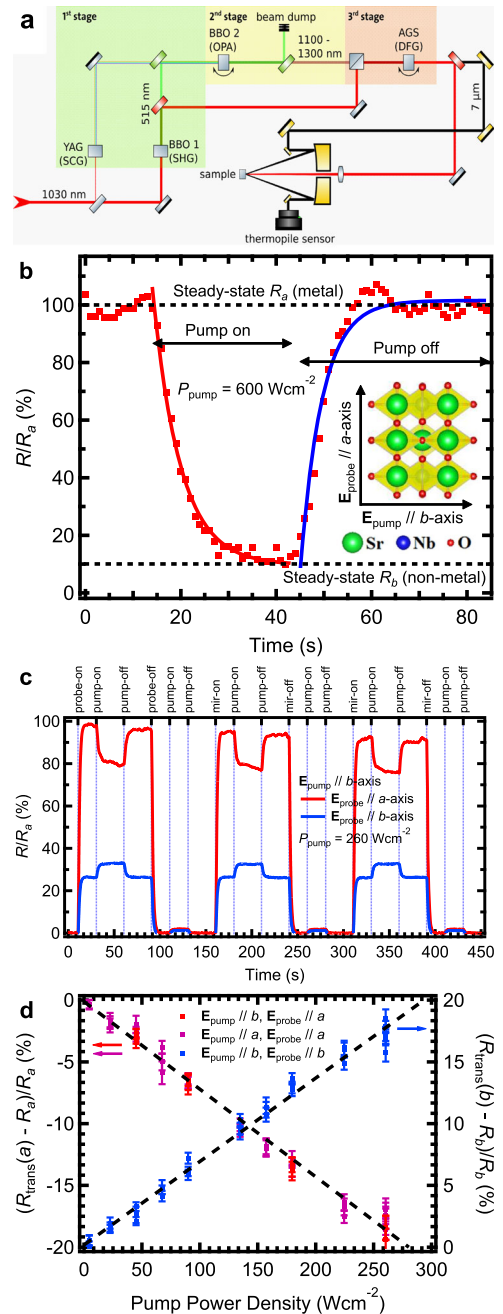


Fig. 4 Photoinduced metastable excitonic insulating state in $n = 5$ type $\text{Sr}_{0.95}\text{NbO}_{3.37}$. **a** Experimental setup of the mid-infrared transient pump-probe experiment with anisotropic pump-probe polarizations. The wavelength of the pump and probe beam is 1030 nm (~ 1.20 eV for the d - d excitons) and $7\ \mu\text{m}$ (~ 0.18 eV), respectively. **b** Near-100% switching of transient reflectance along the a -axis of $n = 5$ type $\text{Sr}_{0.95}\text{NbO}_{3.37}$, $R_{\text{trans}}(a)$, due to the d - d exciton pumping from steady-state metallic level, R_a , all the way down to steady-state insulating level, R_b , indicating a transient photoinduced metal-insulator transition (MIT). The pump polarization, \mathbf{E}_{pump} , is parallel to the b -axis, while the probe polarization, $\mathbf{E}_{\text{probe}}$, is parallel to the a -axis. The pump power density, P_{pump} , is $\sim 600\ \text{Wcm}^{-2}$. **c** Transient reflectance along the a - and b -axes ($R_{\text{trans}}(a)$ and $R_{\text{trans}}(b)$, respectively) of the $n = 5$ type $\text{Sr}_{0.95}\text{NbO}_{3.37}$ sample with various combinations of \mathbf{E}_{pump} and $\mathbf{E}_{\text{probe}}$ polarizations as well as lower P_{pump} values to ensure repeatability of the switching. **d** The P_{pump} dependence of $R_{\text{trans}}(a)$ and $R_{\text{trans}}(b)$ switching, showing the opposite trends of $R_{\text{trans}}(a)$ and $R_{\text{trans}}(b)$ changes as P_{pump} increases. The ranges of \pm standard deviation of the relative changes of $R_{\text{trans}}(a)$ and $R_{\text{trans}}(b)$ are shown by the error bars.

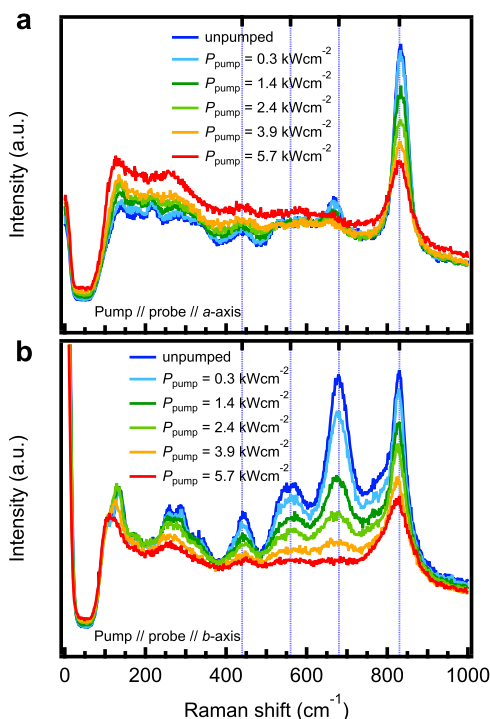


Fig. 5 Transient pump-probe Raman spectroscopy of $n = 5$ type

$\text{Sr}_{0.95}\text{NbO}_{3.37}$. **a** Pump-probe transient Raman spectroscopy of the $n = 5$ type $\text{Sr}_{0.95}\text{NbO}_{3.37}$ sample with varied pump power density, P_{pump} , and pump-probe polarizations parallel to the a -axis. **b** Pump-probe transient Raman spectroscopy of the sample with varied P_{pump} and pump-probe polarizations parallel to the b -axis. The wavelength of the pump, reflectance probe, and Raman probe beam is 1030 nm (-1.20 eV for the d - d excitations), $7 \mu\text{m}$ (-0.18 eV), and 260 nm (-4.77 eV), respectively. Vertical blue dotted lines indicate the Raman modes related to oxygen chains at 830 , 560 , 680 , and 440 cm^{-1} .

pump-probe ultraviolet Raman spectroscopy of phonons in $\text{Sr}_{0.95}\text{NbO}_{3.37}$. The pump beam is 1030 nm (1.20 eV) to match the d - d excitons and the incoming probe wavelength is 260 nm (4.77 eV) matching the $\text{O-}2p \rightarrow \text{Nb-}4d$ charge-transfer inter-band transition edge (see Fig. 2) to address the effects of oxygen and charge orderings. The resulting Raman spectrum with Raman pump and probe polarizations along the b -axis (Fig. 5a) without pumping shows dominant phonon modes located at 440 , 560 , 680 , and 830 cm^{-1} . These modes are consistent with oxygen-bond-related modes observed in many different cuprate superconductors such as single-chain $\text{YBa}_2\text{Cu}_3\text{O}_{6.7}$ (ref. 25), double-chain $\text{YBa}_2\text{Cu}_4\text{O}_8$ (ref. 26), and spin-ladder compounds²⁷. Meanwhile, along the a -axis (Fig. 5b), only the 830 cm^{-1} mode can be distinctly observed, while the rest are suppressed. According to Fig. 1a, b, the Nb–O–Nb bonds along the metallic a -axis are chain-like, while along the insulating b -axis they are zig-zag-like. Thus, as the 440 , 560 , and 680 cm^{-1} modes are observed only along the b -axis but not along the a -axis, these modes are signatures of the zig-zag-like bonds but not the chain-like bonds.

When the exciton pumping is turned on, all these zig-zag-like-related phonon modes decrease dramatically with increasing P_{pump} , indicating that the pumping changes the lattice orderings of the Nb–O–Nb bonds particularly along the b -axis. These decreases can already be observed even at the lowest P_{pump} of 300 Wcm^{-2} . At the highest P_{pump} of 5.7 kWcm^{-2} , the zig-zag-like-related modes become either severely diminished or completely bleached, and the shape of the Raman spectrum along the b -axis approaches that of along the a -axis. This indicates that the

zig-zag-like Nb–O–Nb bonds along the b -axis are transformed by the d - d exciton pumping into more chain-like bonds, which facilitates easier hoppings between Nb ions and increases the conductivity of the normally insulating b -axis, making the a - and b -axes more isotropic consistent with pump-probe MIR-reflectance results. Note that other effects, such as screening of phonon modes by the excited photoelectrons and thermal heating by the laser pump, are unlikely to play significant roles in the evolution of the transient Raman spectra, as discussed in more detail in “Methods” and Supplementary Discussion.

Discussion

As mentioned, transient states caused by electronic and/or excitonic excitations typically have ultrashort lifetime in the pico- to femtoseconds range. Thus, the seconds-long ultraslow recovery time of the transient MITs in Fig. 4 indicates that the typically ultrafast excitonic excitations couple to additional mechanisms that have very slow recovery time. We believe that there are mainly two mechanisms that are responsible for this ultraslow recovery time.

First, as discussed above, the d - d exciton pumping causes the zig-zag-like Nb–O–Nb ordering along the b -axis to transform into more chain-like bonds. As this transient IMT involves changes in the lattice structure, this is an important reason for the slow recovery time along the b -axis, as recovery of lattice structure changes is typically orders of magnitude slower than recovery of electronic transitions.

For the long-lasting transient MIT along the a -axis, we are proposing a mechanism, in which the d - d exciton photo-pumping causes the conversion of most of the free electrons into excitons, depleting the red Nb- $4d$ band in Fig. 3a, causing the decrease of the a -axis metallicity, and creating a large density of excitons. Due to the much lower effective mass of excitons (compared to atomic mass), this large density of excitons can undergo Bose–Einstein-like condensation (BEC) even at room temperature^{10–12,28,29}, similar to what has been observed in the case of photo-pumped magnons in yttrium–iron–garnet films¹³. The coherence of the BEC phase can lead to a very long lifetime of the transient insulating state. For example, in photo-pumped magnons¹³, non-BEC phase decays quickly within 100 – 200 ns while the BEC phase stays coherent even after 1200 ns .

Note that these two mechanisms (changes in the lattice orderings and BEC-like phase transition) may very well be coupled, as together they resemble the signatures of excitonic insulators, a manifestation of exciton BEC in which the insulating ground state is dominated by BEC of excitons accompanied by changes in the lattice orderings^{28,29}. Similar behaviors have been predicted and suspected to be observed in the two likely candidates for intrinsic excitonic insulators: semiconducting Ta_2NiSe_5 (ref. 30) and semimetal $1T\text{-TiSe}_2$ (ref. 31).

Furthermore, with high enough pump power density of 600 Wcm^{-2} , the switching can be made to be nearly 100%, promising potential applications in future photoinduced switching devices such as exciton-based transistors and other optoelectronic devices in general. This is especially important because so far, many other photoinduced systems have only been able to be optically switched by $<35\%$ (refs. 32–35), and/or need high switching power density requirements of $>10^5$ – 10^{10} Wcm^{-2} (refs. 32–37). Thus, the near-100% optical switching of $\text{Sr}_{1-y}\text{NbO}_x$, which only needs a very low pump power density of 600 Wcm^{-2} to induce the switching, represents a very big leap compared to other photo-induced systems, conceptually demonstrating that it is possible to optically switch a system to near-100% switching contrast with very low pump power density.

Methods

Sample preparation. Melt-grown crystalline $n = 4.5$ type $\text{SrNbO}_{3.45}$ and Sr- and O-deficient $n = 5$ type $\text{Sr}_{0.95}\text{NbO}_{3.37}$ samples are prepared by melting, reducing, and solidifying the corresponding fully oxidized Nb^{5+} compositions of $\text{SrNbO}_{3.50}$ and $\text{Sr}_{0.95}\text{NbO}_{3.45}$ under a flow of 98% Ar + 2% H_2 gas¹⁴. The process is done in a GERO mirror furnace where two polycrystalline sintered rods with fully oxidized Nb^{5+} compositions of $\text{SrNbO}_{3.50}$ and $\text{Sr}_{0.95}\text{NbO}_{3.45}$, respectively, are processed by floating zone melting. The two polycrystalline sintered rods themselves are prepared by mingling an appropriate molar ratio of SrCO_3 and Nb_2O_5 , which is then pre-reacted at an elevated temperature in air. After the pre-reaction, the mixture is ground into powder, once again mingled, pressed into the shape of two rectangular rods, and sintered at an elevated temperature in air. The experimental approaches, types, and design of used equipment, devices, and constructions are similar to those which are presented comprehensively in ref. 38. The GERO mirror furnace is presented in Appendix 1 of ref. 38. Photo images of melt-grown crystalline pieces of $n = 4.5$ type $\text{SrNbO}_{3.45}$ and non-stoichiometric $n = 5$ type $\text{Sr}_{0.95}\text{NbO}_{3.37}$ are shown in Supplementary Fig. 1. Pieces of the crystalline samples are then cleaved into flat plate shapes so that their surfaces are parallel to the c -axis (verified with X-ray diffraction, see below). A transmission electron microscopy (TEM) image of $n = 4.5$ type $\text{SrNbO}_{3.45}$ is shown in ref. 14.

X-ray diffraction. The cleaved plate-shaped $n = 5$ type $\text{Sr}_{0.95}\text{NbO}_{3.37}$ and $n = 4.5$ type $\text{SrNbO}_{3.45}$ samples are measured using high-resolution X-ray diffraction to characterize their lattice structures and verify the orientation of their cleaved surfaces. The measurements are done using a Huber 4-circle diffractometer system 90000-0216/0 at Singapore Synchrotron Light Source with a selected X-ray wavelength equal to that of Cu $\text{K}\alpha_1$ radiation ($\lambda = 1.5406 \text{ \AA}$). The resulting $2\theta/\theta$ XRD patterns of both samples are shown in Supplementary Fig. 2. Each major peak in both patterns is a higher-order mode of the (001) Bragg peak, which means that the surface normal of both samples are parallel to the c -axis. Further analysis results in a c -axis lattice constant of 32.404 and 59.300 Å for $\text{Sr}_{0.95}\text{NbO}_{3.37}$ and $\text{SrNbO}_{3.45}$, respectively, consistent with previous results^{14,16}.

Mueller-matrix spectroscopic ellipsometry. As the $\text{Sr}_{1-y}\text{NbO}_x$ samples are highly anisotropic quasi-1D metals, an advanced form of ellipsometry called Mueller-matrix spectroscopic ellipsometry is needed to unambiguously probe their principal dielectric functions along all optical axes^{22–24}. Mueller matrix is a 4×4 matrix unique to each material that describes the changes in light polarizations due to the complex dielectric response of said material²³. Conventional optical absorption spectroscopy techniques typically only measure a few elements of this matrix, making them suitable only for probing isotropic materials. In contrast, Mueller-matrix spectroscopic ellipsometry measures the majority of these elements (in some cases all), enabling us to precisely probe the principal dielectric tensors of highly anisotropic materials along all orthogonal directions. More information and a basic introduction about Mueller-matrix spectroscopic ellipsometry are given in Supplementary Methods.

In this study, the Mueller-matrix spectroscopic ellipsometry measurements are done from 0.38 to 6.10 eV using a Woollam V-VASE ellipsometer with a compensator and rotating analyzer. The cleaved samples are mounted on a precision rotation stage (Newport RS40) to perform azimuth-dependent measurements, where the in-plane rotation angle, φ , is varied from 0° to 315° in steps of 45° . At each in-plane orientation, the measurements of each Mueller-matrix element, m_{ij} , are done at three incident angles, θ , of 50° , 60° , and 70° from the sample surface normal. Such an angle-resolved measurement scheme is necessary to ensure a complete characterization of arbitrary optically anisotropic samples^{22–24}. This setup is capable of measuring 12 out of the 16 Mueller-matrix elements (from m_{11} to m_{34}), which is sufficient to obtain the principal ϵ of highly anisotropic samples.

The resulting incident-angle-, azimuth-dependent Mueller-matrix element spectra are analyzed using the Woollam WVASE software. The fitting parameters are the principal ϵ of the samples along the major optical axes and the Euler angles of α , β , and γ . The principal dielectric functions, ϵ_a , ϵ_b , and ϵ_c along the a -, b -, and c -axis, respectively, are modeled using the Kramers–Kronig transformable Drude²³ and Herzinger–Johs Psemi-Tri³⁹ oscillator functions. Meanwhile, real-valued and wavelength-independent Euler angles describe the rotation between the Cartesian laboratory frame of (x, y, z) and the samples' Cartesian optical axis frame of (a, b, c) : α represents a rotation around the z -axis to rotate from (x, y, z) to (x', y', z) , β represents a rotation around the x' -axis to rotate from (x', y', z) to (x', y'', z) , and γ represents a rotation around the z' -axis to rotate from (x', y'', z) to (a, b, c) . The samples' surface roughnesses ($\sim 8 \text{ nm}$ for $n = 5$ type $\text{Sr}_{0.95}\text{NbO}_{3.37}$ and $\sim 5 \text{ nm}$ for $n = 4.5$ type $\text{SrNbO}_{3.45}$) are modeled by a Bruggeman-mode effective medium approximation²³ with 50% material and 50% void ($\epsilon_{\text{void}} = 1 + i0$).

The analysis is done using non-linear regression methods, where measured and calculated Mueller-matrix elements are matched until the mean-squared error (MSE) between the fit and the data is minimized. Each sample is analyzed in a multi-sample configuration analysis scheme²⁴, where data from all in-plane orientations and incident angles are included in the regression analysis and only the azimuthal Euler angle of α is set according to the in-plane rotation measurement configuration ($\varphi_{n+1} = \varphi_n + 45^\circ$, thus α is also set such that $\alpha_{n+1} = \alpha_n + 45^\circ$). The Mueller-matrix spectroscopic ellipsometry spectra are measured in

an extended energy setup: the extended infrared part from 0.38 to 1.00 eV and the infrared-visible-ultraviolet part from 0.60 to 6.10 eV, both in steps of 0.02 eV. In the regression analysis, these two parts are fit simultaneously to obtain the complete principal ϵ from 0.38 to 6.10 eV. As representative examples, the comparisons between measured and fitted Mueller-matrix elements after the final fit for $\varphi = 0^\circ, 45^\circ, 90^\circ$, and 135° ; $\theta = 70^\circ$; and energy range of 0.6–6.1 eV are shown in Supplementary Fig. 3 (for $\text{Sr}_{0.95}\text{NbO}_{3.37}$) and Supplementary Fig. 4 (for $\text{SrNbO}_{3.45}$).

The resulting principal ϵ of $\text{Sr}_{0.95}\text{NbO}_{3.37}$ and $\text{SrNbO}_{3.45}$ are shown in Figs. 1 and 2. The analysis also reveals that the Euler angle of β of both samples is very small ($<0.1^\circ$ for $\text{Sr}_{0.95}\text{NbO}_{3.37}$ and 0.6° for $\text{SrNbO}_{3.45}$), indicating that the optical c -axis of the samples coincides with their respective surface normal and thus, per XRD results (Supplementary Fig. 2), with their respective crystallographic c -axis. These minute β also mean that the Euler angles of α and γ are practically equivalent (since the z -axis is almost unchanged by the rotation of β), and the combined angle of $\alpha + \gamma$ can be used to determine the orientation of the a - and b -axis with respect to the plane of incident (POI) at a given φ . For $\text{Sr}_{0.95}\text{NbO}_{3.37}$ at $\varphi = 0^\circ$, the a -axis (b -axis) is oriented at -11.8° (78.2°) from the intersection line between the POI and the sample surface. Meanwhile, for $\text{SrNbO}_{3.45}$ at $\varphi = 0^\circ$, the a -axis (b -axis) is oriented at -8.4° (81.6°) from the intersection line between the POI and the sample surface.

Excitonic ultraviolet Raman spectroscopy. Ultraviolet Raman spectroscopy measurements of excitons are performed with the UT-3 Raman spectrometer⁴⁰ with 1800 s integration time. The 240 nm probe beam is obtained by frequency tripling of a Tsunami Ti:Sapphire laser (model 3950-X1BB, Spectra Physics Lasers Inc., repetition rate: 80 MHz) with a spot size of 15 μm and a power of 5.8 mW. The spectral response of the spectrometer is calibrated using a certified white light calibration lamp from Gigahertz Optik (DKD).

Density functional theory calculations. Density functional theory (DFT) calculations are done using the Perdew–Burke–Ernzerhof⁴¹ (PBE96) exchange–correlation potential and the projector-augmented wave (PAW) method⁴² as implemented in the Vienna ab initio simulation package⁴³ (VASP). In these calculations, Sr-4s4p5s, Nb-4p5s4d, and O-2s2p orbitals are treated as valence states, employing the PAW potentials labeled as “Sr_sv”, “Nb_sv”, and “O” in the VASP PBE library. The cutoff energy for the plane-wave basis set is set to 500 eV and the partial occupancies for each orbital use the Gaussian smearing with a width of 0.2 eV. The atomic structure of $n = 5$ type $\text{SrNbO}_{3.4}$ is taken from experimentally determined atomic positions in ref. 16 which is modeled by supercells containing 54 atoms with a space group of $Pnmm$. The band structure is calculated with $23 \times 17 \times 3$ Γ -centered Monkhorst–Pack k -point meshes. The Fermi level is adjusted so that it is consistent with previous electrical transport, ARPES, and infrared reflectivity results^{17–19}. The calculated band structure of $\text{SrNbO}_{3.4}$ near the Fermi level is presented in Fig. 3a, while the extended version down to $E - E_F = -7.5 \text{ eV}$ is shown in Supplementary Fig. 5a. Note that in the extended version, the deep-lying O-2p band is located below $E - E_F = -3 \text{ eV}$, rather than -4 eV , according to the UPS results¹⁷, due to the well-known Kohn–Sham bandgap underestimation problem in DFT. Similar DFT calculation results of $\text{SrNbO}_{3.4}$ that showed the O-2p bands have also been reported previously in ref. 17.

Angular-resolved photoemission spectroscopy (ARPES). The ARPES measurements were performed at the SUV beamline⁴⁴ of Singapore Synchrotron Light Source (SSLS) using a Scienta-Omicron DA30L electron analyzer. The single crystalline sample of $\text{Sr}_{0.95}\text{NbO}_{3.37}$ is cleaved inside the load lock chamber under pressure 5×10^{-8} mbar using the standard top-post method. The sample is then immediately transferred to the analysis chamber with base pressure 1×10^{-10} mbar. The measurements were performed at room temperature using helium lamp source (photon energy = 21.21 eV). An ARPES cut of the $n = 5$ type $\text{Sr}_{0.95}\text{NbO}_{3.37}$ sample along the a - (Γ - X) and b -axis (Γ - Y) is presented in Fig. 3b and Supplementary Fig. 5b, respectively. The ARPES cut along the a -axis (b -axis) is taken at $k_y = 0$ ($k_x = 0$) to ensure that there is no momentum contribution along the b -axis (a -axis). The ARPES cut along the Γ - Y direction shows a weak and non-dispersive band between $E_B = -(E - E_F) = 0.2 \text{ eV}$ and 0.6 eV , consistent with the DFT calculation in Fig. 3a that also shows non-dispersive bands at around $E - E_F = -0.5 \text{ eV}$ along the Γ - Y direction. Meanwhile, the Fermi surface map (Fig. 3c) is obtained using the electrostatic deflection lensing functionality of a DA30L analyzer without rotating the sample.

Mid-infrared transient pump-probe reflectivity. Since Mueller-matrix spectroscopic ellipsometry shows an onset of the Drude response for energies of the order of $\sim 1 \text{ eV}$ in the metallic direction, the reflectance of a laser-based mid-infrared (MIR) beam with a wavelength of 7 μm ($\sim 0.18 \text{ eV}$) probes predominantly the free electronic carriers associated to the Drude response. The main source laser for the MIR-reflectance setup (c.f., Fig. 4a) is a fiber amplified laser (Tangerine HP, 35 W) supplying typically 300 femtosecond pulses with 70 μJ at a 50 kHz repetition rate into the difference frequency generation setup as described by the following stages. The 1st stage is a supercontinuum generation in a YAG-crystal and second harmonic generation in a beta barium borate (BBO) type 1 crystal with 1030 nm

pump. The 2nd stage is an optical parametric amplification of 515 nm pump and supercontinuum seed in BBO type 2 crystal to generate a near-infrared beam of 1100–1300 nm. The 3rd stage is a differential frequency generation of 1030 nm pump and near-infrared seed in an AGS-crystal to generate a MIR beam of 6–12 μm . The MIR beam is focused on the sample using an on-axis parabolic mirror. The pump beam is focused on the sample through a hole in the same parabolic mirror. The reflected intensity is recorded using a thermopile power sensor (Coherent PS10). Spot diameter sizes of ~ 0.3 mm are determined by knife-edge experiments of pump and probe beams. The wavelength of the probe is measured with an integrated FTIR-spectrometer utilizing a pyroelectric sensor. Pump-on and pump-off are switched by an optical shutter. Data shown in Fig. 4b, c are real-time measurements of the observed reflected intensity.

The pump-on relaxation time constant, τ_{on} , is fitted from the red solid curve in Fig. 4b using

$$R_{\text{trans}}(t) = y_0 + Ae^{\left(\frac{t-t_0}{\tau_{\text{on}}}\right)} \quad (1)$$

where t_0 is the turn-on time point, y_0 is the background level to which R_{trans} approaches as time, t , goes to infinity if the pump is perpetually turned on, and A is the amplitude of the R_{trans} change. Meanwhile, the pump-off relaxation time constant, τ_{off} , is fitted from the blue solid curve in Fig. 4b using

$$R_{\text{trans}}(t) = y_0 + A \left[1 - e^{\left(\frac{t-t_0}{\tau_{\text{off}}}\right)} \right] \quad (2)$$

For both fittings, y_0 and A are identical within the error bars. From this analysis, τ_{on} and τ_{off} is estimated to be 5.8 ± 0.2 s and 4.6 ± 0.2 s, respectively.

Transient pump-probe Raman spectroscopy. Raman spectroscopy measurements are performed using the UT-3 Raman Spectrometer⁴⁰ with 300 s integration time. The 260 nm probe beam is obtained by frequency tripling of a Tsunami Ti:Sapphire laser (model 3950-X1BB, Spectra Physics Lasers Inc., repetition rate: 80 MHz) with a spot size of 15 μm and a power of 2.8 mW. The 1030 nm pump beam is provided by a Tangerine fiber laser (Amplitude Systemes, repetition rate: 500 kHz) with a spot size of 50 μm . The power of the pump beam is varied between 10 and 70 mW with a polarizer $\lambda/2$ -waveplate combination, also controlling the polarization of the pump beam. The polarization of the probe beam is fixed, and the relative polarization with respect to the sample axes is varied by rotating the sample. Spatial overlap is ensured by imaging the laser focus on the sample. Since transient reflectivity measurements show timescales longer than the repetition rate of the laser systems, there is no need for temporal overlap of the laser pulses.

The effects of thermal heating from the pump laser are estimated by studying the changes in width and frequency of the phonon modes as a function of pump power density. This is because according to the anharmonic decay model⁴⁵, the linewidth of phonons is dependent on the temperature and thereby a good indicator for heating effects (Supplementary Fig. 6). From this we derive that the heating effect for pump power densities of up to 300 Wcm^{-2} is equivalent to an increase in temperature of <50 K, since there is no significant change in the linewidth for this power density. Heating only becomes significant (in terms of increasing the sample temperature) for pump power densities above 1 kWcm^{-2} , which are used only for pump-probe Raman but not for pump-probe MIR reflectance.

Data availability

The data that support the findings of this study are available from the corresponding authors upon reasonable request.

Code availability

The theoretical band structure is calculated using the openly-available VASP program and the implementation codes are available from the corresponding authors upon reasonable request.

Received: 5 July 2020; Accepted: 16 September 2020;

Published online: 10 November 2020

References

- Collet, E. et al. Laser-induced ferroelectric structural order in an organic charge-transfer crystal. *Science* **300**, 612–615 (2003).
- Ichikawa, H. et al. Transient photoinduced ‘hidden’ phase in a manganite. *Nat. Mater.* **10**, 101–105 (2011).
- Rini, M. et al. Control of the electronic phase of a manganite by mode-selective vibrational excitation. *Nature* **449**, 72–74 (2007).
- Hilton, D. J. et al. Enhanced photosusceptibility near T_c for the light-induced insulator-to-metal phase transition in vanadium dioxide. *Phys. Rev. Lett.* **99**, 226401 (2007).
- Ehrke, H. et al. Photoinduced melting of antiferromagnetic order in $\text{La}_{0.5}\text{Sr}_{1.5}\text{MnO}_4$ measured using ultrafast resonant soft X-ray diffraction. *Phys. Rev. Lett.* **106**, 217401 (2011).
- Först, M. et al. Spatially resolved ultrafast magnetic dynamics initiated at a complex oxide heterointerface. *Nat. Mater.* **14**, 883–888 (2015).
- Zong, A. et al. Evidence for topological defects in a photoinduced phase transition. *Nat. Phys.* **15**, 27–31 (2019).
- Fausti, D. et al. Light-induced superconductivity in a stripe-ordered cuprate. *Science* **331**, 189–191 (2011).
- Mitrano, M. et al. Possible light-induced superconductivity in K_3C_{60} at high temperature. *Nature* **530**, 461–464 (2016).
- Einstein, A. Quantentheorie des einatomigen idealen Gases. *Zweite Abhandlung. Sitz. ber. Preuss. Akad. Wiss.* **1**, 3–14 (1925).
- Blatt, J. M., Böer, K. W. & Brandt, W. Bose-Einstein condensation of excitons. *Phys. Rev.* **126**, 1691–1692 (1962).
- Moskalenko, S. A. & Snoke, D. W. *Bose-Einstein Condensation of Excitons and Biexcitons and Coherent Nonlinear Optics with Excitons* (Cambridge University Press, 2000).
- Demokritov, S. O. et al. Bose-Einstein condensation of quasi-equilibrium magnons at room temperature under pumping. *Nature* **443**, 430–433 (2006).
- Lichtenberg, F., Herrnberger, A., Wiedenmann, K. & Mannhart, J. Synthesis of perovskite-related layered $\text{A}_n\text{B}_n\text{O}_{3n+2} = \text{ABO}_x$ type niobates and titanates and study of their structural, electric and magnetic properties. *Prog. Solid State Chem.* **29**, 1–70 (2001).
- Isawa, K., Sugiyama, J., Matsuura, K., Nozaki, A. & Yamauchi, H. Synthesis and transport properties of Sr_xNbO_3 ($0.75 \leq x \leq 0.90$). *Phys. Rev. B* **47**, 2849–2853 (1993).
- Abrahams, S. C. et al. Centrosymmetric or noncentrosymmetric? Case study, generalization and structural redetermination of $\text{Sr}_2\text{Nb}_2\text{O}_{17}$. *Acta Cryst. B* **54**, 399–416 (1998).
- Kuntscher, C. A. et al. Electronic structure of layered perovskite-related $\text{Sr}_{1-y}\text{La}_y\text{NbO}_{3.5-x}$. *Phys. Rev. B* **61**, 1876–1883 (2000).
- Kuntscher, C. A. et al. Extremely small energy gap in the quasi-one-dimensional conducting chain compound $\text{SrNbO}_{3.41}$. *Phys. Rev. Lett.* **89**, 236403 (2002).
- Kuntscher, C. A. et al. Electronic and vibrational properties of the low-dimensional perovskites $\text{Sr}_{1-y}\text{La}_y\text{NbO}_{3.5-x}$. *Phys. Rev. B* **70**, 245123 (2004).
- Chen, C. et al. Atomic-scale origin of the quasi-one-dimensional metallic conductivity in strontium niobates with perovskite-related layered structures. *ACS Nano* **11**, 12519–12525 (2017).
- Akishige, Y., Kobayashi, M., Ohi, K. & Sawaguchi, E. Dielectric and ferroelectric properties in the low temperature phase of strontium niobate. *J. Phys. Soc. Jpn.* **55**, 2270–2277 (1986).
- Schubert, M. Polarization-dependent optical parameters of arbitrarily anisotropic homogeneous layered systems. *Phys. Rev. B* **53**, 4265–4274 (1996).
- Fujiwara, H. *Spectroscopic Ellipsometry: Principles and Applications* (Wiley, 2007).
- Schmidt, D., You, L., Chi, X., Wang, J. & Rusydi, A. Anisotropic optical properties of rhombohedral and tetragonal thin film BiFeO_3 phases. *Phys. Rev. B* **92**, 075310 (2015).
- Bahrs, S. et al. Anisotropic ultraviolet Raman resonance in underdoped $\text{YBa}_2\text{Cu}_3\text{O}_{6.7}$. *Phys. Rev. B* **74**, 024519 (2006).
- Bäckström, J. et al. Raman scattering in $\text{YBa}_2\text{Cu}_4\text{O}_8$ and $\text{PrBa}_2\text{Cu}_4\text{O}_8$: indications of pseudogap effects in nonsuperconducting $\text{PrBa}_2\text{Cu}_4\text{O}_8$. *Phys. Rev. B* **61**, 7049–7054 (2000).
- Rusydi, A. et al. Experimental observation of the crystallization of a paired holon state. *Phys. Rev. Lett.* **105**, 026402 (2010).
- Jérome, D., Rice, T. M. & Kohn, W. Excitonic insulator. *Phys. Rev.* **158**, 462–475 (1967).
- Kohn, W. & Sherrington, D. Two kinds of bosons and Bose condensates. *Rev. Mod. Phys.* **42**, 1–11 (1970).
- Lu, Y. F. et al. Zero-gap semiconductor to excitonic insulator transition in Ta_2NiSe_5 . *Nat. Commun.* **8**, 14408 (2017).
- Kogar, A. et al. Signatures of exciton condensation in a transition metal dichalcogenide. *Science* **358**, 1314–1317 (2017).
- MacDonald, K. F., Sámson, Z. L., Stockman, M. I. & Zheludev, N. I. *Ultrafast Act. Plasmon. Nat. Photon.* **3**, 55–58 (2009).
- Sámson, Z. L., MacDonald, K. F. & Zheludev, N. I. Femtosecond active plasmonics: ultrafast control of surface plasmon propagation. *J. Opt. A: Pure Appl. Opt.* **11**, 114031 (2009).
- Abb, M., Albella, P., Aizpurua, J. & Muskens, O. L. All-optical control of a single plasmonic nanoantenna-ITO hybrid. *Nano Lett.* **11**, 2457–2463 (2011).
- Vasa, P. et al. Real-time observation of ultrafast Rabi oscillations between excitons and plasmons in metal nanostructures with J-aggregates. *Nat. Photon.* **7**, 128–132 (2013).
- Wurtz, G. A. et al. Designed ultrafast optical nonlinearity in a plasmonic nanorod metamaterial enhanced by nonlocality. *Nat. Nanotech.* **6**, 107–111 (2011).
- Wu, H.-Y. et al. Ultrasmall all-optical plasmonic switch and its application to superresolution imaging. *Sci. Rep.* **6**, 24293 (2016).

38. Lichtenberg, F. *Presentation of a Laboratory for the Synthesis and Study of Special Oxides and Melt-grown Crystalline Materials*. <https://doi.org/10.3929/ethz-a-010817148> (ETH Zurich, 2017).
39. Johs, B., Herzinger, C. M., Dinan, J. H., Cornfeld, A. & Benson, J. D. Development of a parametric optical constant model for $\text{Hg}_{1-x}\text{Cd}_x\text{Te}$ for control of composition by spectroscopic ellipsometry during MBE growth. *Thin Solid Films* **313–314**, 137–142 (1998).
40. Schulz, B., Bäckströmb, J., Budelmann, D., Maeser, R. & Rübhausen, M. Fully reflective deep ultraviolet to near infrared spectrometer and entrance optics for resonance Raman spectroscopy. *Rev. Sci. Instrum.* **76**, 073107 (2005).
41. Perdew, J. P., Burke, K. & Ernzerhof, M. Generalized gradient approximation made simple. *Phys. Rev. Lett.* **77**, 3865–3868 (1996).
42. Kresse, G. & Joubert, D. From ultrasoft pseudopotentials to the projector augmented-wave method. *Phys. Rev. B* **59**, 1758–1775 (1999).
43. Kresse, G. & Furthmüller, J. Efficient iterative schemes for ab initio total-energy calculations using a plane-wave basis set. *Phys. Rev. B* **54**, 11169–11186 (1996).
44. Yu, X. J., Diao, C. Z., Venkatesan, T., Breese, M. B. H. & Rუსyди, A. A soft x-ray-ultraviolet (SUV) beamline and diffractometer for resonant elastic scattering and ultraviolet-vacuum ultraviolet reflectance at the Singapore synchrotron light source. *Rev. Sci. Instrum.* **89**, 113113 (2018).
45. Klemens, P. G. Anharmonic decay of optical phonons. *Phys. Rev.* **148**, 845–848 (1966).

Acknowledgements

The authors thank Nicola Spaldin, Joël Mesot, and Peter Abbamonte for useful discussions and various support as well as Jason Chee Wai Lim for technical support. The crystalline niobate samples were prepared at the University of Augsburg and F.L. thanks German Hammerl, Alexander Herrnberger, Thilo Kopp, Jochen Mannhart, and Klaus Wiedenmann for their support. The authors also thank the Singapore Synchrotron Light Source (SSLS) for providing the facility necessary for conducting the research. SSLS is a National Research Infrastructure under the Singapore National Research Foundation. This work was supported by the Singapore National Research Foundation under its Competitive Research Funding (No. NRF-CRP 8-2011-06 and No. R-398-000-087-281), MOE-AcRF Tier-2 (MOE2015-T2-1-099, MOE2015-T2-2-065, and MOE2015-T2-2-147), NUS YIA, MOE-AcRF Tier-1 (R-144-000-423-114, R-144-000-398-114, R-144-000-388-114 and R-144-000-439-114), and NUS Core Support (C-380-003-003-001). The work at Hamburg by M.R, F.B., B.G.L., and S.B. was supported by BMBF via VUVFAST (05K14GUB) and DFG via RU773/8-1.

Author contributions

T.C.A., M.A.N., and A.R. performed Mueller-matrix spectroscopic ellipsometry measurements and analysis. F.L. prepared the crystalline niobate samples. F.B., P.L., S.B.,

B.G.L., A.R., and M.R. set up and performed pump-probe mid-infrared reflectance and ultraviolet Raman spectroscopy measurements. T.Z., P.E.T., and A.R. performed theoretical band structure calculations. P.K.D., T.C.A., and A.R. performed ARPES measurements. P.Y. and T.C.A. performed X-ray diffraction measurements. A.D.F., C.D., and A.R. performed X-ray absorption spectroscopy experiment for checking the samples surface quality and orientation. T.C.A. and A.R. predicted and proposed the metal-insulator transitions induced by excitonic excitations. A.R. and T.C.A. analyzed the data comprehensively and wrote the paper with inputs from all co-authors including D.W., M.B.H.B., and T.V. A.R. and T.C.A. initiated, planned, and coordinated the project. A.R. led the project.

Competing interests

The authors declare no competing interests.

Additional information

Supplementary information is available for this paper at <https://doi.org/10.1038/s42005-020-00451-w>.

Correspondence and requests for materials should be addressed to T.C.A., M.R. or A.R.

Reprints and permission information is available at <http://www.nature.com/reprints>

Publisher's note Springer Nature remains neutral with regard to jurisdictional claims in published maps and institutional affiliations.



Open Access This article is licensed under a Creative Commons Attribution 4.0 International License, which permits use, sharing, adaptation, distribution and reproduction in any medium or format, as long as you give appropriate credit to the original author(s) and the source, provide a link to the Creative Commons license, and indicate if changes were made. The images or other third party material in this article are included in the article's Creative Commons license, unless indicated otherwise in a credit line to the material. If material is not included in the article's Creative Commons license and your intended use is not permitted by statutory regulation or exceeds the permitted use, you will need to obtain permission directly from the copyright holder. To view a copy of this license, visit <http://creativecommons.org/licenses/by/4.0/>.

© The Author(s) 2020